Sensors & Actuators: B. Chemical 439 (2025) 137762

Contents lists available at ScienceDirect

Sensors and Actuators: B. Chemical

journal homepage: www.elsevier.com/locate/snb

Rotating mirror short-wave infrared hyperspectral imaging system: Characterization and applications

José A. Gutiérrez-Gutiérrez [a], Verónica Mieites [a,b], José M. López-Higuera [a,b,c], Olga M. Conde [a,b,c,*]

[a] Grupo de Ingeniería Fotónica (Dep. TEISA), Universidad de Cantabria, Avenida de los Castros, Santander, 39007, Cantabria, Spain
[b] Instituto de Investigación Marqués de Valdecilla (IDIVAL)., Avenida Cardenal Herrera Oria s/n,, Santander, 39011, Cantabria, Spain
[c] CIBER-BBN, Calle de Melchor Fernández Almagro, 3, 28029, Madrid, Spain

ARTICLE INFO

Keywords:
Hyperspectral imaging
Short-wave infrared
Rotative mirror
Liquid phantoms
biological phantoms

ABSTRACT

Hyperspectral imaging (HSI) is a powerful analytical tool with broad applicability across diverse fields, including agriculture, biomedicine, and industry. This article introduces a new custom hyperspectral device that operates in the SWIR (Short-Wave InfraRed) range (900-1700 nm). Based on a previously tested design featuring a rotating mirror, this device opens new possibilities for the physicochemical characterization of tissues and materials. This equipment provides up to 5 nm spectral resolution and 176.8×111.36 μm^2 spatial resolution, without moving the equipment or the sample. Key features of the device are detailed, and a dual validation method is presented: using reference spectra to their concentrations and using reference concentrations to estimate their spectra. Validation is carried out through the quantitative analysis of liquid mixtures and the qualitative analysis of biological specimens. The proposed HSI system extends the capabilities of the technique into the SWIR range, offering strong potential for its application in diverse biomedical and industrial scenarios.

1. Introduction

Hyperspectral imaging (HSI) is a chemical imaging tool able to characterize materials on a large number of channels, or wavelengths, within specific spectral ranges. Particularly, the Short-Wave Infrared (SWIR) spectral range, beyond the visible spectrum, reveals unique fingerprints of various molecules based on their vibrational properties, favoring non-destructive and label-free analysis, and providing valuable insights into the chemical composition of diverse materials and biological samples [1,2].

The applications of HSI-SWIR systems are varied and noteworthy. It has been applied to alloy inspection of fine metal particles from vehicle recycling and contaminant detection [3]. In the food industry, the SWIR range is useful for quality assessment of products like meat, since protein and fat peaks are detected in this range [4]. Additionally, HSI-SWIR is useful in detecting false smut disease in rice [5], in assessing seed viability [6–8], and in discriminating between abiotic and biotic drought stress caused by nematodes in tomato plants [9]. Furthermore, this spectral range is employed in selecting fertilized eggs and removing non-fertilized or poorly fertilized ones [10], as well as in the rapid, non-destructive detection of melamine in milk powder [11]. Other applications of HSI-SWIR include the evaluation of paintings to reveal underdrawings, hidden details, and characterizing artists' materials [12], and biomedical applications such as diagnosing skin allergies, especially in individuals with dark skin, where the SWIR range is particularly effective since it bypasses the coloration caused by melanin [13,14].

Spectral imaging systems are classified based on the number of bands they capture: hyperspectral imaging systems contain hundreds of bands, and multispectral imaging (MSI) systems contain tens of bands.

Several authors have provided detailed descriptions of the construction of spectral devices in the SWIR range. For example, Kutteruf et al. [15] present a nine-channel SWIR system with a filter array on the sensor, achieving a resolution of 40 nm. Steiner et al. [16] describe an MSI-SWIR system for facial recognition using a ring of LEDs at four different wavelengths, with spectral resolutions between 65 and 130 nm.

Some hyperspectral imaging systems are based on wavelength scanning by using tunable sources [17], or liquid crystal filters on the sensor or on a white light source. In particular, Wang et al. developed a SWIR hyperspectral wavelength-scanning system with liquid crystal tunable filters achieving spectral resolutions ranging from 10 to 32 nm, depending on the scanned wavelength [18]. Pushbroom systems, which are

* Corresponding author at: Grupo de Ingeniería Fotónica (Dep. TEISA), Universidad de Cantabria, Avenida de los Castros, Santander, 39007, Cantabria, Spain.
E-mail addresses: gutierrja@unican.es (J.A. Gutiérrez-Gutiérrez), olga.conde@unican.es (O.M. Conde).

https://doi.org/10.1016/j.snb.2025.137762
Received 28 August 2024; Received in revised form 4 April 2025; Accepted 4 April 2025
Available online 17 April 2025

Table 1
Summary of features for some SWIR systems. The comparison includes spectral resolution (SR), number of spectral bands (SB), spatial resolution (SpR), and potential portability (Port.).

System	SR [nm]	SB	SpR [μm]	Port.
Kutteruf et al. [15]	40	9	>1000	High
Steiner et al. [16]	65–130	4	>1000	High
Wang et al. [18]	10–32	23–75	25	Low
Lee et al. [11]	5.9	287	400 × 100	Low
Fabelo et al. [19]	5	172	128.7 × 480	Medium

an alternative to wavelength scanning systems, use diffractive optics to decompose an imaging line into its spectrum with high spectral resolution. Pushbroom-based configurations achieve a large number of bands and high resolution across a wide spectral range. These systems generally need to move the sample, or the system itself, using motorized stages to scan the second spatial dimension. In Lee et al.'s work [11], they use an HSI-SWIR system with a platform that moves the sample, offering a spectral resolution of 5.9 nm within the range of 1000 to 2500 nm.

In some applications, like in the biomedical ones that take place in the operating room, it is not possible to move the patient, and the only suitable option is to move the imaging system. In the work of Fabelo et al. [19], where they use several HSI systems during surgical interventions, a scanning platform moves the cameras to obtain two-dimensional images with a spectral resolution of 5 nm over 172 bands.

Nevertheless, operating theatres are often cramped and lack the space for bulky setups. As an alternative, snapshot systems can capture a spectral image without the need for any type of scanning by using color filter arrays on the sensor. However, there is a tradeoff between the number of filters and the spatial resolution: as the number of filters increases, the spatial resolution decreases accordingly [20].

Another relevant characteristic for these systems is their compact form factor. Tran and Fei [21] define a compact HSI as one that weighs no more than 5 kg and does not require cables or additional components. An ultra-compact system is defined as one that does not exceed 500 g . The advantage of a compact or ultra-compact system is that, in addition to leaving space for other instruments, it offers simple setup and operation, which is crucial for many end-user applications.

Portability is defined as the system's ability to be moved. Portability is considered low when the system is anchored to a fixed structure, requiring all samples to be placed in a specific location. Portability is medium when the system is mounted on a movable structure, allowing better adaptability to different situations. Finally, portability is considered high when the system can potentially be mounted on a tripod or even handheld without the need for additional structures. Table 1 summarizes the characteristics of some of the systems found in the literature.

In this work, we present an HSI system with medium portability that utilizes a rotating mirror and operates in the SWIR range. Based on our previous work [22], this rotating mirror design, originally developed for an HSI system in the visible-near-infrared (VisNIR) range, has now been completely adapted and characterized for the new spectral range. The main advantage is that, by using a rotating mirror, there is no need to move the system nor the sample, while keeping a small footprint. The proposed system offers high spectral and spatial resolution over the SWIR range (900–1700 nm), with over 200 spectral bands. The objective is to characterize its spatial and spectral resolution and validate its use with liquid phantoms and biological samples, demonstrating its potential for biomedical applications.

2. Materials and methods

This section outlines the equipment, the liquid and biological phantom preparation, and the developed methodologies to ensure the effective operation of the imaging system.

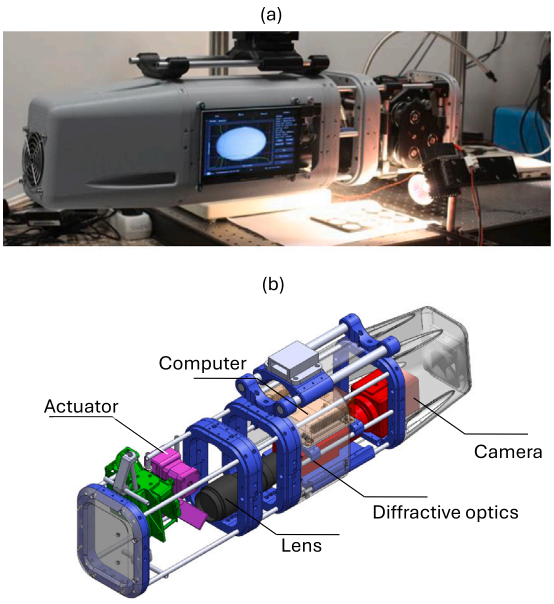

Fig. 1. Proposed HSI-SWIR system: (a) photograph of the setup and light source; (b) schematic of the setup. The system contains a camera, diffractive optics, a macro lens and an actuator module with a rotating mirror. An onboard computer controls each subsystem to configure and synchronize the measurements and to store the data.

2.1. Imaging system setup

The hyperspectral imaging system utilizes a scanning camera featuring a rotating mirror. Fig. 1 shows a photograph and a diagram of its components, detailed below:

Imaging subsystem. The camera, a Xeva 1.7–320 (Xenics, Belgium), is equipped with an InGaAs sensor that provides a resolution of 320 × 256 pixels between 900 nm and 1700 nm and 12-bit depth. It is coupled with a diffractive element (ImSpector N17E, Specim, Spectral Imaging Ltd., Finland) that provides a theoretical spectral resolution of 5 nm, and a Navitar lens (Navitar Inc., IL, USA) with 18 to 108 mm focal length.

Actuator subsystem. Features a servomotor that drives the rotating mirror. The setup includes a DRV 8825 motor driver (Texas Instruments Inc., TX, USA), a NEMA 17 stepper motor (CUI Devices, Lake Oswego, OR, USA), and a three-stage gear. An Arduino Uno serves as the microcontroller, orchestrating the mirror positioning via USB commands from the control subsystem. This subsystem divides the 360° rotation of the mirror into 19200 steps (53 steps per degree). The system is configured to work within the angular range from 22° to 67°, corresponding to steps between 1173 and 3573, where the characterization procedure has shown that field of view linearity is achieved, [22].

Control subsystem. Managed by a barebone computer (MSI Cubi *N* 8GL-001BEU-BN4000XX, Micro-Star International, Co., Ltd, New Taipei City, Taiwan) with an Intel Celeron N4000 processor, 8 GB of memory, and 128 GB internal storage.

Software. The control software running on a custom Linux distribution is designed to optimize measurement control and data storage. It supports remote connectivity for user terminals and integration with applications based on wireless devices.

During operation, the control subsystem communicates with both the camera and the actuator subsystem. Upon receiving a command, the Arduino adjusts the mirror to a specified angle. The camera then captures a frame to generate an image represented as $X \times \lambda$, where X is the first spatial coordinate and λ is the spectral coordinate. The data

is temporarily stored in memory until it is transferred to a high-speed NVMe solid state drive, freeing up memory for continuous measurements. The spectral hypercube is obtained by rotating the mirror over the observation scene to add the second spatial coordinate Y, thus forming the final hyperspectral cube $X \times Y \times \lambda$, with a maximum resolution of 320x2400x232.

2.2. Optical measurements

The diffuse reflectance, which represents the percentage of light diffusely reflected by a sample, is measured by the HSI-SWIR system. Two distinct measurements are required to obtain the diffuse reflectance: one to acquire the radiation coming from the sample itself, and another of the radiation coming from a reference standard. This procedure is necessary to decouple the system's response and the light source's response from the samples' response. The dark current noise of the system must also be measured [23,24]. The exposure time set for the sample and for the reference measurements does not need to be the same, thus, the diffuse reflectance R is defined as:

$$R = \frac{I - b_I}{I_0 - b_{I_0}} \cdot \frac{t_{I_0}}{t_I}, \tag{1}$$

where I is the intensity of the sample, b_I is the dark current noise of the sample's measurement, I_0 is the intensity of the reference, b_{I_0} is the dark current noise of the reference's measurement, t_I is the exposure time of the sample, and t_{I_0} is the exposure time of the reference. Notice that R will take values from 0 to 1 due $I_0/t_{I_0} > I/t_I$ and $b_I/t_I \simeq b_{I_0}/t_{I_0}$.

In the case of non-turbid samples (without scattering), the Beer–Lambert law is used to relate diffuse reflectance to the absorption coefficient of the material [25]. The absorption coefficient models the loss of light power as it propagates through a medium as

$$I(z) = I_0 e^{-\mu_a z}, \tag{2}$$

where μ_a is the absorption coefficient of the medium, z is the optical path length, I_0 is the illumination intensity, and $I(z)$ is the intensity after the light has passed through the optical path z. In this case, the diffuse reflectance from Eq. (1) is related to the Beer–Lambert law Eq. (2) as follows:

$$\mu_a = -\frac{1}{z} ln(R) = -\frac{1}{z} ln\left(\frac{I - b_I}{I_0 - b_{I_0}} \cdot \frac{t_{I_0}}{t_I}\right). \tag{3}$$

The system's dark current noise is the minimum intensity that can be measured (in pixel counts). The dark current noise in the light source measurement may not coincide with that of the sample measurement, as it depends on the exposure time. The minimum reflectance that the equipment can measure, with $t_{I_0} > 0$, is defined as:

$$R_{\min} = \lim_{I \to b_I} \left(\frac{I - b_I}{I_0 - b_{I_0}} \cdot \frac{t_{I_0}}{t_I}\right). \tag{4}$$

On the other hand, the maximum reflectance that can be measured corresponds to those pixel counts near the saturation point of the sample, defined as

$$R_{\max} = \lim_{I \to 2^N - 1} \left(\frac{I - b_I}{I_0 - b_{I_0}} \cdot \frac{t_{I_0}}{t_I}\right), \tag{5}$$

where N is the bit depth of the sensor, and therefore $2^N - 1$ is the maximum count level the system can provide. In this case, the camera is 12 bits, so the maximum count is 4095.

However, in practice, neither the sample measurements nor the reference measurements will reach levels close to saturation. This is because the system works with the aperture nearly closed to ensure the image is well-focused, and the exposure time cannot exceed 500 ms due to camera limitations. Under optimal lighting conditions, the reference measurements reach about 50% of the camera's dynamic range with the nearly closed aperture settings.

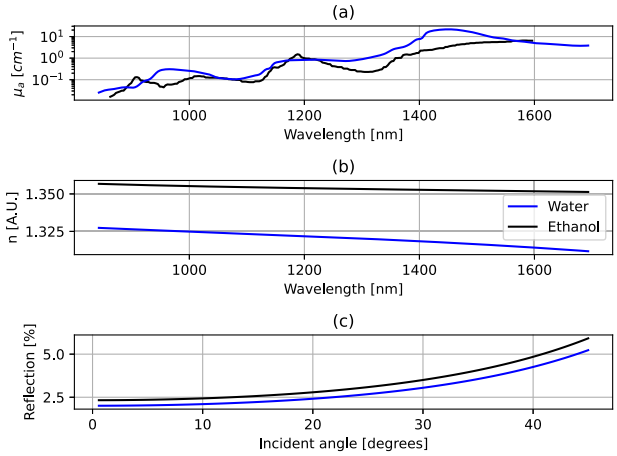

Fig. 2. Optical properties of ethanol and water: (a) absorption coefficient; (b) refractive index; (c) Fresnel's reflection as a function of the angle of incidence [26–29].

2.3. Liquid phantom design

To assess the accuracy of the HSI-SWIR system, a semi-transparent liquid phantom with varying concentrations of water and ethanol was prepared. This phantom appears transparent under visible light, yet is distinctly translucent in the SWIR range.

It is essential to consider the spectral dependence of μ_a for the individual chemical components used for the preparation of liquid phantoms. These differences, which are detectable within the SWIR spectral range for the water-ethanol phantoms, will modify the total absorption of the mixture. Fig. 2 displays optical properties in the SWIR range of water and ethanol: Fig. 2(a) shows the absorption coefficient of ethanol and water as published in literature; Fig. 2(b) depicts their refractive index and Fig. 2(c) displays the Fresnel's reflection as a function of the angle of incidence [26–29].

The exposure time restricts the maximum and minimum measurable reflectance (Eq. (5), Eq. (4)), and thus, the feasible depth of these phantoms. Deep phantoms would result in high absorption, thus reducing system sensitivity, while shallow phantoms in combination with lower absorption ranges would prevent the system from quantifying it effectively. The maximum and minimum optical path can be quantified as

$$\begin{cases} z_{\max} = -\frac{1}{\mu_{a,\max}} \ln(R_{\min}), \\ z_{\min} = -\frac{1}{\mu_{a,\min}} \ln(R_{\max}), \end{cases} \tag{6}$$

where z_{max} and z_{min} represent the maximum and minimum optical paths that the equipment can measure, $\mu_{a,max}$ is the maximum absorption coefficient and $\mu_{a,min}$ is the minimum one [30].

Due to the refractive index change between the air and the liquid phantom, two effects occur when a light ray strikes the surface at a specific angle: Fresnel's reflection and refraction. The latter affects the optical path length. Fig. 3 illustrates the path of a light ray striking the phantom surface at an angle θ_1. In Fig. 3, n_1 is the refractive index of air, n_2 is that of the medium, θ_1 is the angle of incidence of a light ray, θ_2 is the refracted angle, z_i is the path length of light between the entrance of the medium and the bottom, z_r is the path length of the light ray collected by the sensor from the bottom to the exit of the medium, X_i is the point of incidence of the light, and X_r is the point where the light exits the medium. The geometrical path z_g, knowing that $z_g = z_i + z_r$ and that $z_r = h$, is then calculated as follows:

$$z_g(\theta_1, n_1, n_2) = h\left(\sqrt{\frac{-n_2^2}{n_1^2 \sin^2(\theta_1) - n_2^2}} + 1\right). \tag{7}$$

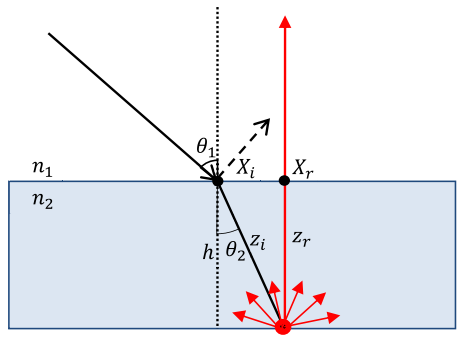

Fig. 3. Diagram of the optical path on the sample, given an angle of incidence of the light source and some refractive indices and a surface that causes a diffuse reflection, the optical path to follow is one, assuming that the normal ray to the surface is collected by the image system.

Table 2
Absorption coefficient (μ_a) (900 nm - 1700 nm), refractive index (n) [31], limits of optical path (Z) and height limits (h) for an angle of incidence $\theta_1 = \pi/4$ and I_0 of 2048 counts.

	$\mu_a[\lambda]$ (cm^{-1})	$n[\lambda]$	$Z[\lambda]$ (mm)	$h[\lambda]$ (mm)
H_2O	0.10- 21.58	1.31–1.32	0.01–1.74	0.003-0.6
EtOH	0.06–6.51	0.02–6.74	1.34–1.35	0.01-2.28

Since the first medium is air, we assume $n_1 = 1$. Therefore, z_g becomes a function only of θ_1 and n_2. The geometrical path can also be expressed as the sum of the path traveled by a light ray when it strikes the surface perpendicularly and an additional increment caused by the actual angle of incidence. The path traveled by the light when the angle is perpendicular to the surface is twice the height of the phantom, $z_g(0, n_2) = 2h$, so the geometrical path can be expressed as:

$$z_g(\theta_1, n_2) = z_g(0) + \Delta z_g(\theta_1, n_2) = 2h + \Delta z_g(\theta_1, n_2), \tag{8}$$

where Δz_g is defined as:

$$\Delta z_g(\theta_1, n_2) = h\left(\sqrt{\frac{-n_2^2}{\sin^2(\theta_1) - n_2^2}} - 1\right). \tag{9}$$

Thus, the optical path can be expressed as:

$$z(\theta_1, n_2) = n_2 z_g(\theta_1, n_2) = n_2(2h + \Delta z_g(\theta_1, n_2)). \tag{10}$$

Given the optical path and the optical properties of water and ethanol, displayed in Fig. 2, Table 2 includes the optical path limits and, consequently, the limiting heights of the phantom that the system can measure, considering a noise level of approximately 50 counts out of 4095, an incidence angle of 45°, a reference level I_0 of 2048 counts out of 4095, and an exposure time of 500 ms.

For their construction, the custom-designed 3D printed wells were used. The wells were printed in polylactide plastic (PLA) with a Prusa P3Steel 3D printer. These wells were coated with matte black Pintyplus paint (NOVASOL SPRAY, S.A., Spain), with their bases finished in matte white to enhance the diffuse reflectance measurement.

Due to the technical limitations of the employed printer, the final height of the wells is 1 mm with a diameter of 30 mm. Although the diameter does not influence the measurements, it allows us to take enough points in the image, obtaining a large number of spectra ($> 10^5$) of each phantom. This way, we can obtain the volume of the wells as

$$V = \pi\left(\frac{D}{2}\right)^2 h = 706.86\ \text{mm}^3 = 706.86\ \mu\text{L}. \tag{11}$$

For the experiment, 8 different mixtures of 96% ethanol and water were prepared. The measurement process is illustrated in Fig. 4. Each phantom was measured in the same well, starting with 100% water and then alternating between different concentrations of water and ethanol.

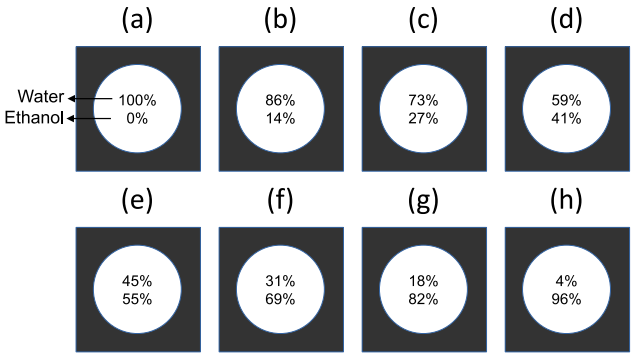

Fig. 4. Schematics of the measurements made on a 1mm well with different liquid phantom compositions. The top number indicates water concentration, bottom number indicates ethanol ones, sorted by measurement sequence from (a) to (h). All measurements were conducted with 500 ms exposure time at 4 °C for 3 min.

The well was thoroughly dried between measurements to prevent potential cross-contamination of the mixtures. The liquid phantoms were stored in a refrigerator at 4 °C, and each measurement did not exceed 3 minutes, minimizing the likelihood of significant evaporation.

2.4. Corrected absorption coefficient

Relating the variations in optical path length with the absorption coefficient and diffuse reflectance, we obtain the following relationship [25,32]:

$$\mu_a z = \mu_a n(2h + \Delta z_g) = -\ln(R). \tag{12}$$

However, as previously explained, when light hits a material with a different refractive index than air at a certain angle, the angle is modified, and part of the light is reflected according to Fresnel's equations:

$$R_p = \left|\frac{n_1\cos\theta_1 - n_2\cos\theta_2}{n_1\cos\theta_1 + n_2\cos\theta_2}\right|^2 \tag{13}$$

$$R_s = \left|\frac{n_1\cos\theta_2 - n_2\cos\theta_1}{n_i\cos\theta_2 + n_2\cos\theta_1}\right|^2 \tag{14}$$

$$R_{\text{eff}} = \frac{1}{2}(R_s + R_p) \tag{15}$$

where θ_1 is the angle of incidence, θ_2 is the angle of transmission, n_1 is the refractive index of the first medium (usually air), n_2 is the refractive index of the second medium (a mixture of water and ethanol), R_p is the p-polarized light reflection, R_s is the s-polarized light reflection, and R_{eff} is the effective reflection when assuming the incident light is unpolarized (natural light). The angle θ_2 is substituted using Snell's law as:

$$\theta_2 = \sqrt{1 - \left(\frac{n_1}{n_2}\sin\theta_1\right)^2}, \tag{16}$$

so that the specular reflection is only a function of the refractive index and the angle of incidence.

By incorporating the specular reflection, we modify Eq. (1) as follows:

$$R = e^{-\mu_a z} = (1 + R_{\text{eff}})\frac{I - b_I}{I_0 - b_{I_0}}. \tag{17}$$

The introduction of Fresnel's reflection models the light loss upon incidence, which is about 2% when the angle is normal to the surface, and reach up to 4.5% for a 45° angle.

We define a term β as the natural logarithm of $1 + R_{\text{eff}}$, such that $\beta = \ln(1 + R_{\text{eff}})$, to simplify the calculations. Using Eqs. (12) and (17),

we obtain:

$$\mu_a = -\frac{1}{z} ln(R) = \\ = -\frac{1}{n_2(2h+\Delta z_g)} \left[\ln\left(\frac{I - b_I}{I_0 - b_{I_0}} \right) + \beta \right]. \quad (18)$$

With this model, we relate I, β and Δz to the absorption coefficient. In this case, the model is treated as a linear fit where all the terms are simplified as follows:

$$\mu_a = -aX + b, \quad (19)$$

where

$$a = -\frac{1}{n_2(2h+\Delta z_g)}, \\ X = \ln\left(\frac{I - b_I}{I_0 - b_{I_0}} \right), \\ b = -\frac{1}{n_2(2h+\Delta z_g)}\beta.$$

2.5. Spectrum and concentration estimation

The total absorption coefficient of a sample is related to the absorption coefficients of its pure components which, for the case of biological samples, are available in the literature [33–37]. Therefore, the total absorption coefficient is expressed as a sum of the several substances' absorption coefficients, each multiplied by a volume fraction [32], as follows:

$$\mu_a = \sum_{i=0}^{N} \varphi_i \mu_{a,i}, \quad (20)$$

where μ_a is the total absorption coefficient, φ_i the volume fraction, and $\mu_{a,i}$ the absorption coefficient of each of the compounds in the mixture. For a mixture of water and ethanol, this is rewritten as:

$$\mu_a = \varphi_{H_2O}\mu_{\mathrm{a},\ H_2O} + \varphi_{\mathrm{EtOH}}\mu_{\mathrm{a,EtOH}}, \quad (21)$$

where the subindex H_2O represents water and, EtOH, ethanol.

Having multiple samples with known concentrations, one can establish multiple equations that relate the absorption coefficient to the different concentrations. Using least squares regression, the pure spectra are estimated. Conversely, with known pure spectra, the concentrations of mixtures are determined.

2.6. Biological phantom

In addition to the liquid phantoms of water and ethanol, a biological phantom has been developed using minced chicken breast meat and pork lard. The objective is to validate the system for fat content detection by observing spectral changes in the SWIR region (900–1700 nm) as the fat content increases. Fat content is used a disease biomarker in muscular dystrophy [38] atherosclerosis [39,40] or fatty liver disease [41].

The most relevant chromophores in these mixtures are water and fat, as tissues consist of approximately 70 % water. Spectrally, water and fat exhibit significant differences, as shown in Fig. 5. It might be assumed that the spectra of a meat-fat mixture can be decomposed using the absorption coefficients shown in Fig. 5 by means of Eq. (20). However, it is not possible to directly estimate the absorption coefficient of this meat-fat mixture, nor its optical path length due, to its high scattering, which should not be ignored even in the SWIR range.

Alternatively, an analysis based on peaks and valleys enables the identification of spectral differences between water and fat. Specifically, water peaks at 970, 1170, and 1450 nm, and lipid peaks at 927, 1030, 1211, and 1390 nm, along with their respective valleys, provide optimal reference points. Based on these spectral characteristics, a ratio between the diffuse reflectance at two wavelengths can be defined, which is related to the fat concentration, as expressed by

$$K = \frac{R(\lambda = \lambda_{fat})}{R(\lambda = \lambda_{water})}, \quad (22)$$

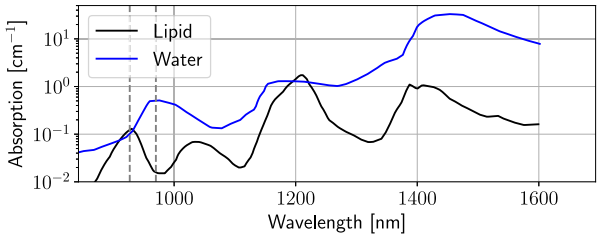

Fig. 5. Reference spectra of lipids and water in the SWIR region [42]. Vertical lines at 927 and 970 nm have been marked as these wavelengths are of interest for this work.

Table 3
The mass of each component used to create the mixtures is shown. A portion of each mixture was extracted and reweighed before being measured.

	M1 (g)	M2 (g)	M3 (g)	M4 (g)	M5 (g)
Chicken	36.929	18.214	8.933	4.86	0
Fat	0	6.45	9.041	14.828	17.644
Portion	17.556	15.585	16.834	17.265	17.644

Table 4
Volume fractions calculated for each mixture using the density of chicken breast as $\rho_{muscle} = 1.06$ g/mL and the density of pork lard as $\rho_{fat} = 0.9196$ g/mL [43].

	M1 (%)	M2 (%)	M3 (%)	M4 (%)	M5 (%)
Chicken	100	71.03	46.16	22.14	0
Fat	0	29	54.84	77.96	100

where R represents the diffuse reflectance, λ_{fat} corresponds to a wavelength where fat exhibits a valley, λ_{water} is the wavelength where water exhibits a valley, and K is the ratio of the corresponding two diffuse reflectances.

As observed in Fig. 5, the wavelength of 970 nm is a strong candidate for λ_{fat}, as water exhibits a peak in this region while lipids present a valley. Complementarily, 927 nm is a suitable choice for λ_{water}, where fat shows a peak and water displays reduced absorption.

Different mixtures of minced chicken breast and pork lard were prepared, with their proportions detailed in Table 3, as well as the initial mass of each component and the amount used for the measurements.

Taking as reference the density of muscle tissue $\rho_{muscle} = 1.06$ g/mL and adipose (fat) tissue $\rho_{fat} = 0.9196$ g/mL [43], the volume fraction of each component in the mixtures can be calculated using the equation:

$$\varphi_i = \frac{m_i/\rho_i}{m_i/\rho_i + m_j/\rho_j}, \quad (23)$$

where φ_i is the volume fraction of component i, m_i is its mass, ρ_i is its density, and j represents the values of the other component in the mixture. The volume fractions for each phantom prepared with meat and fat are presented in Table 4.

3. Results

This section presents the results of our study. First, we describe the characterization of the HSI-SWIR equipment, in terms of the obtained spatial resolution using a USAF chart, and the spectral resolution achieved with a set of tunable lasers. Then, we describe the spectral calibration of the equipment using two different methods.

We have evaluated how specular reflection and optical path length vary, as well as the estimation of volume fractions in the prepared liquid phantoms. Changes in the specular reflection and the optical path have led to the observed variations in the spectrum, which has been characterized both statistically and through 2D imaging maps.

Finally, we present several application examples on biological tissues and chemical components, demonstrating the capabilities of this equipment in assessing the biological and tissue compositions.

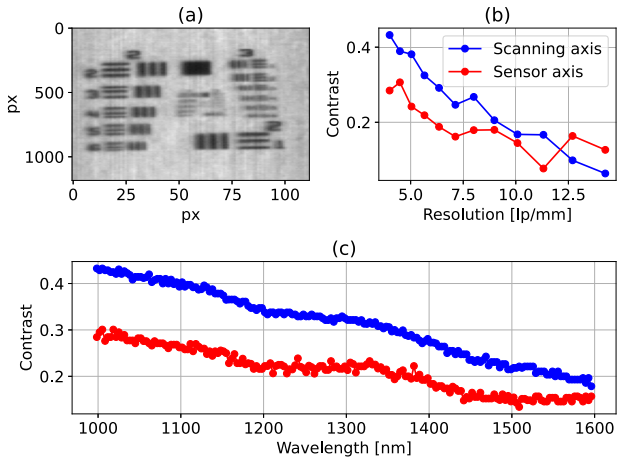

Fig. 6. Contrast measurement using a 1951 USAF chart: (a) USAF chart; (b) image contrast as a function of resolution for both vertical and horizontal axes at 1000 nm; (c) contrast as a function of wavelength at 4 lp/mm.

3.1. Spatial resolution and field of view

The lens and diffractive optics assembly function together as a macro lens. At approximately 5 cm above the image plane, we achieve a sharp image, so we used this value as the working distance. The field of view (FoV) varies between 2 × 10 cm and 10 × 10 cm, depending on the zoom setting used or, in other words, between 22° and 90°. To characterize the spatial resolution, a 1951 USAF resolution test chart was used, assessing the contrast, both vertically and horizontally, in lines per millimeter (lp/mm). Fig. 6(a) shows part of USAF chart reflectance acquired at 1000 nm.

The USAF chart is divided in groups (g) and elements (e) which were used to calculate the contrast transfer function of the system (CTF). Let $I_{80\%}$ be the 80th percentile of the intensity values of each group-element, $I(g,e)$, and $I_{20\%}$ its 20th percentile. Then, the contrast is calculated as

$$\mathrm{CTF}(g,e) = \frac{I_{80\%}(g,e) - I_{20\%}(g,e)}{I_{80\%}(g,e) + I_{20\%}(g,e)}. \tag{24}$$

By avoiding using the outlier values of each $I(g,e)$ distribution, spurious effects due to hot or dead pixels are not included in the contrast calculations [44].

The groups and elements of the USAF chart are related to the spatial resolution (R_{xy}) as follows

$$R_{xy} = 2^{g+\frac{e-1}{6}}, \tag{25}$$

derived in lp/mm. Fig. 6(b) displays the contrast as a function of lp/mm at 1000 nm and the contrast as a function of wavelength at 4 lp/mm. The spatial resolution differs between the vertical and horizontal lines. This is attributable to the horizontal lines being parallel to the scanning axis, and the vertical lines being parallel to the sensor axis, which has lower resolution.

At 1000 nm, the contrast remains above 0.2 for resolutions less than 5.656 lp/mm on the sensor axis and 8.98 lp/mm on the scanning axis, corresponding to a final resolution of 176.8 × 111.36 μm^2, making this equipment suitable even for small samples. Lastly, Fig. 6(c) shows how the contrast decreases as the wavelength increases (50% approximately), which is predictable according to Rayleigh's criterion [45].

3.2. Spectral calibration and resolution

Spectral calibration in these devices involves establishing a relationship between the sensor position on the spectral axis and its corresponding wavelength [46]. To perform this calibration, two methods were used: a Wavelength Calibration Standard (WCS) (WCS-MC-020 by Labsphere, Inc., North Sutton, NH, USA) and three tunable lasers. The spectral ranges of the lasers are: laser A from 1255 to 1365 nm (HP8168B, Hewlett-Packard Inc., Palo Alto, CA, USA); laser B from 1450 to 1590 nm (HP8168F, Hewlett-Packard Inc., Palo Alto, CA, USA) and laser C from 1580 to 1680 nm (SANTEC TSL-210V, Santec Holdings Corporation, Aichi, Japan). Additionally, an Optical Spectrum Analyzer (OSA) (MS9740 A, Anritsu Corporation, Kanagawa, Japan) was used to record the reference spectra of the different lasers.

Fig. 7(a) shows the three lasers in different colors as recorded by the OSA, all with a spectral bandwidth of approximately 0.1 nm and varying power depending on the laser and wavelength. These lasers were measured by the HSI-SWIR system by reflecting them off a white, diffuse surface (Spectralon®, by Labsphere, Inc., North Sutton, NH, USA), and the intensity of each laser has been divided by its maximum recorded intensity for visualization purposes. The OSA provides enough points (500 points over a 10 nm range) to measure the spectral width of the lasers, whereas the HSI-SWIR equipment represents the laser's spectrum with 3 pixels. The laser peaks do not necessarily align with the sensor, as they may fall between pixels. It is also observed that the normalized intensities match in both the OSA and the HSI, except for Laser C, where there is a sensitivity drop beyond 1650 nm due to the decrease in the sensor's quantum efficiency.

Fig. 7(b) shows the diffuse reflectance measurement of the WCS, compared to the reflectance in the datasheet, along with manually selected points. This selection establishes a relationship between position on the sensor and its wavelength. It is observed that, in the regions below 1000 nm and above 1650 nm, the measured reflectance does not match the theoretical reflectance due to the low quantum efficiency of the sensor in these spectral regions. In areas with good sensitivity, the measured reflectance aligns with the theoretical reflectance with an error of approximately 5%.

Fig. 7(c) shows the relationship between the wavelengths of the lasers measured with the OSA and the sensor position, as well as the pairs obtained from the WCS. Fitting these points with a second-degree polynomial results in the following equation:

$$\hat{\lambda}_i = 4.06 \cdot 10^{-5} p_i^2 + 3.32 p_i + 845.66. \tag{26}$$

where p_i is the pixel position on the sensor and $\hat{\lambda}_i$ is the corresponding wavelength. The second-degree term is five orders of magnitude smaller than the linear term, indicating a high degree of linearity with a Pearson coefficient $R^2_{Pearson}$ greater than 0.99.

In Fig. 7(d), a comparison is made between the spectrum of a laser tuned near 1631 nm, both on the OSA and the HSI-SWIR system. Estimating the bandwidth based on the 3 dB drop, the width reaches approximately half a pixel, suggesting a spectral resolution of 4.6 nm with an uncertainty of ±3.3 nm due to the pixel size. The HSI-SWIR system features an Imspector N17E, whose datasheet specifies a spectral resolution of 5 nm, indicating that the spectral resolution of this equipment is limited by the pixel size on the sensor.

These results indicate high linearity and good system performance, as well as a satisfactory spectral resolution.

3.3. System evaluation with liquid phantoms

Once the equipment was characterized and calibrated, its functionality was evaluated using eight liquid phantoms composed of ethanol and water at different and known concentrations, as described in Section 2.3. After printing and painting the phantom wells, their depth was measured with a caliper, indicating a depth of 0.96 ± 0.02 mm. By applying Eq. (3) for this depth value, with a noise level of 50 counts and a reference intensity of 2000 counts, we calculated the maximum absorption coefficient that the equipment can measure, which is 10 cm^{-1}, approximately.

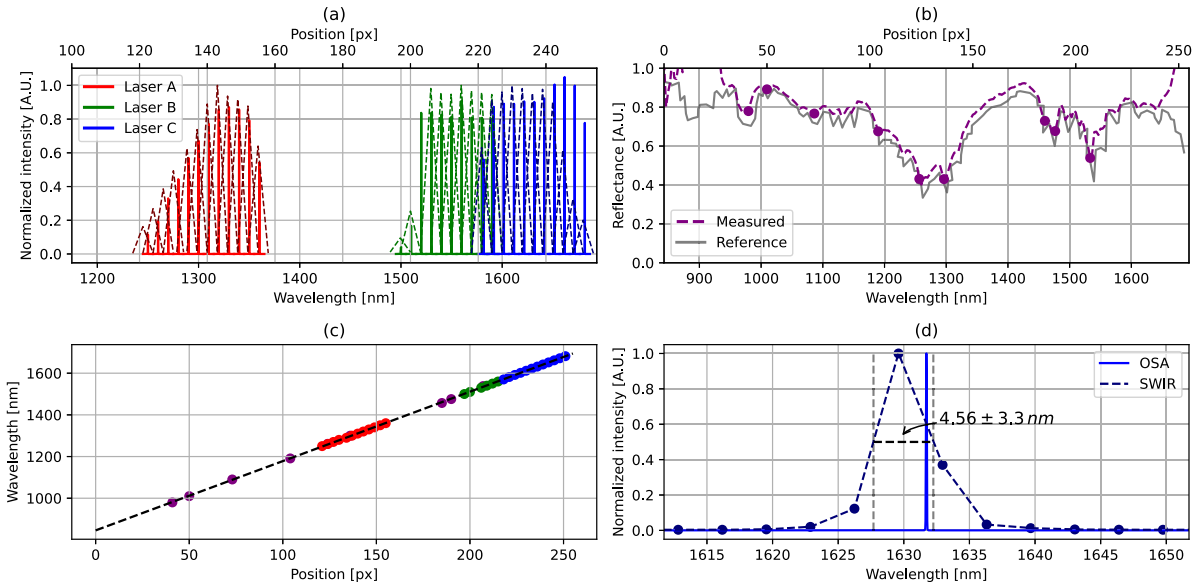

Fig. 7. Spectral calibration and resolution: (a) laser measurements on the OSA and the normalized intensity of the lasers in the HSI system; (b) diffuse reflectance of the WCS measured compared to the theoretical values; (c) relationship between the sensor position and wavelength along with the fitting curve; (d) results of the spectral resolution of the HSI and OSA.

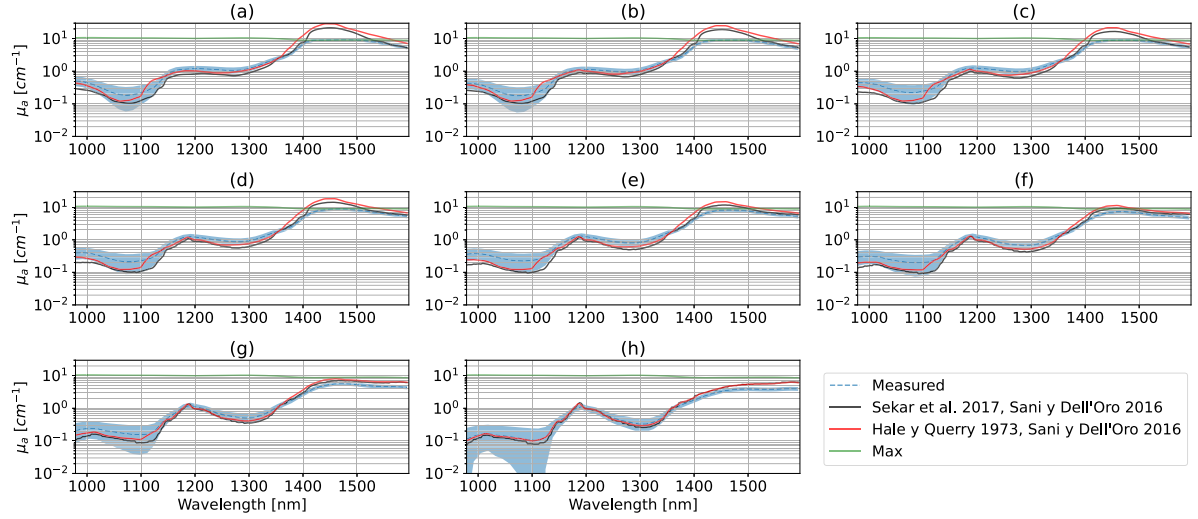

Fig. 8. Measurement of the absorption coefficient of each water-ethanol phantom and its comparison with theoretical values from different sources [26–29]. The shaded area indicates the 95% confidence range of all attenuation coefficient values, when considering the effect of varying β and Δz_g. The green line represents the maximum absorption coefficient that our system can measure. The labels (a-h) of the different spectra correspond to those liquid concentrations shown in Fig. 4.

Knowing the concentrations and spectra of water and ethanol, the values of β and Δz_g for each pixel and each phantom are estimated by fitting the spectra to Eq. (19). These values range from 0.05 to 0.12 for β and from 0.25 to 0.78 mm for Δz_g (with a 2σ, 95% confidence interval). From β, we derive that the specular reflection ranges from 5% to 12%, which implies an incidence angle of 45 ° to 55 °. With an incidence angle of 55 °, theoretically, we expect an increase of 0.25 mm in the optical path length. Any further increase in the optical path length may be attributed to non-optical phenomena, such as the surface tension of the liquids.

Fig. 8 shows the measured spectra for each phantom with varying concentrations of water and ethanol, when tuning the parameters β and Δz_g. The measured spectra are compared with reference spectra from the literature [26–29].

It is seen that the absorption coefficient does not reach the maximum value previously calculated. This is evident in the initial phantoms, where the higher water concentration results in greater absorption in the SWIR spectral range. In spectral regions where absorption is lower, there is more variability in the estimation of the absorption coefficient, indicating reduced precision when the coefficient is smaller. This effect is visually enhanced by the logarithmic representation.

Using the theoretical spectra, the concentrations of water and ethanol are estimated. Fig. 9 shows the concentration estimates for each phantom. In Fig. 9(a) the estimate is shown without any correction parameters; in Fig. 9(b) the estimate is shown using average parameters $\beta = 0.052$ and $\Delta z_g = 0.5$ mm, and in Fig. 9(c) pixel-wise parameters are used. The pixel-wise parameters for a point (x, y) are those obtained by fitting the measured spectrum to the theoretical one based on the given concentrations of ethanol and water.

It is observed that when no correction parameters are used (Fig. 9(a)), the concentration at each point varies due to not considering β and Δz_g. Even on average, the concentration exceeds 1, which has no physical meaning. This does not occur when average parameters are used (Fig. 9(b)), although some data dispersion may still exist.

The results of Fig. 9 are obtained from the hyperspectral images displayed in Figs. 10, 11, and 12. In these figures, the labels (a-h)

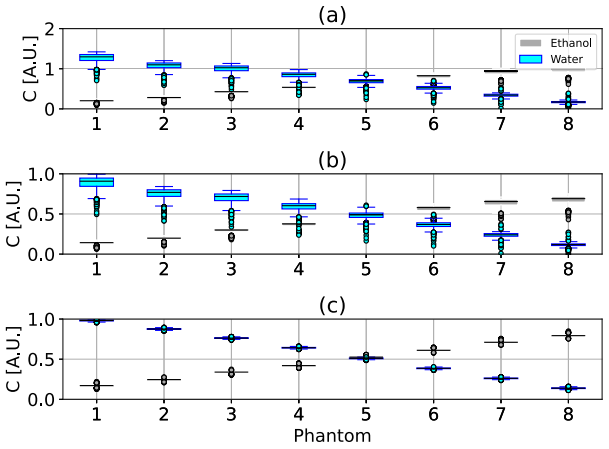

Fig. 9. Estimation of water and ethanol concentrations on the phantom: (a) estimation without correction parameters; (b) estimation with average parameters ($\beta = 0.052$ and $\Delta z_g = 0.5$ mm); (c) estimation with pixel-wise parameters.

correspond to those in the diagram of Fig. 4. Fig. 10 showcases the image equivalent to the boxplots in Fig. 9(a). It is observed that in Fig. 10 (a.0-h.0), the ethanol concentration increases, and in Fig. 10 (a.1-h.1), the water concentration decreases. The concentration appears to be higher in the center than at the edges, indicating that surface tension could indeed be the source of this effect. Additionally, the water concentration exceeds 100% in Fig. 9 and when both concentrations are added in Fig. 10 (a.2-h.2). The MSE between the measured and theoretical spectra is shown in Fig. 10 (a.3-h.3), indicating that it is higher in the center of the well. The increment in MSE in the center could be caused by the flatter surface of the samples at these locations, which creates specular reflections not accounted for in Eq. (21).

Fig. 11 shows the concentration maps that correspond with Fig. 9(b) where the average optical parameters β, Δz_g were used. A similar distribution to the previous case is observed, although with concentrations closer to the theoretical values. This is expected, as the use of average optical parameters does not aim to correct at the pixel level. Finally, in Fig. 12, the concentration maps using pixel-wise optical parameters are shown. Here, the effects of surface tension are compensated for, resulting in a much more homogeneous image across the surface.

From the results, it is concluded that estimating the optical path and surface reflections substantially improves the concentration estimation for liquid mixtures. Furthermore, using parameters at the pixel-wise level corrects for variations in the optical path and the angle of incidence of the light. The proposed pixel-wise model is useful for large-scale quantification of the individual components of any liquid composition of known materials, as long as the mixture does not have a significant scattering contribution.

3.4. Biological phantom results

This subsection presents the results of measurements conducted on the biological phantom made from minced chicken breast meat and pork lard. These phantoms were measured and calibrated using Spectralon® placed at the same height as the sample to characterize their diffuse reflectance. Fig. 13 shows the measurement results, starting with an RGB image where the fat gradient in the meat is visually evident. This is further reflected in the SWIR spectrum, where meat exhibits significantly higher absorption than fat, primarily due to its high water content. Upon analyzing the spectrum, distinct peaks are observed, which become more pronounced as the fat content increases.

As mentioned earlier, the analysis was performed by selecting wavelengths deemed relevant to calculate a ratio (K) related to the fat volume fraction. The results of these ratios are presented in Fig. 14; (a) using boxplot graphs, while (b.1-b.5) shows the results in 2D images.

As seen in Fig. 14, the ratios are directly proportional to the fat volume in each sample, with similar deviations across the samples.

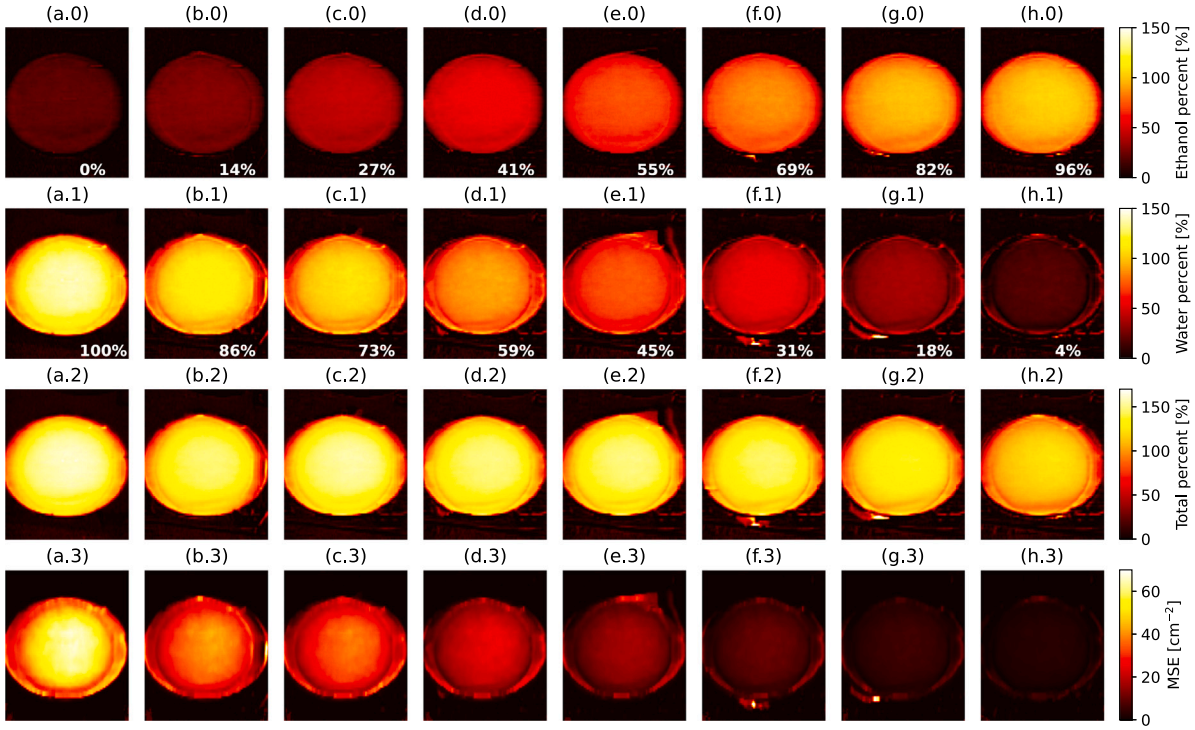

Fig. 10. Results of concentration measurements without using any coefficients. The images have been labeled following Fig. 4: (a.0-h.0) ethanol concentrations; (a.1-h.1) water concentrations; (a.2-h.2) concentrations of the ethanol and water mixture; (a.3-h.3) MSE (Mean Squared Error) of the absorption coefficient fit to Eq. (20). Each row has its own colorbar, which is shared across all images within that row.

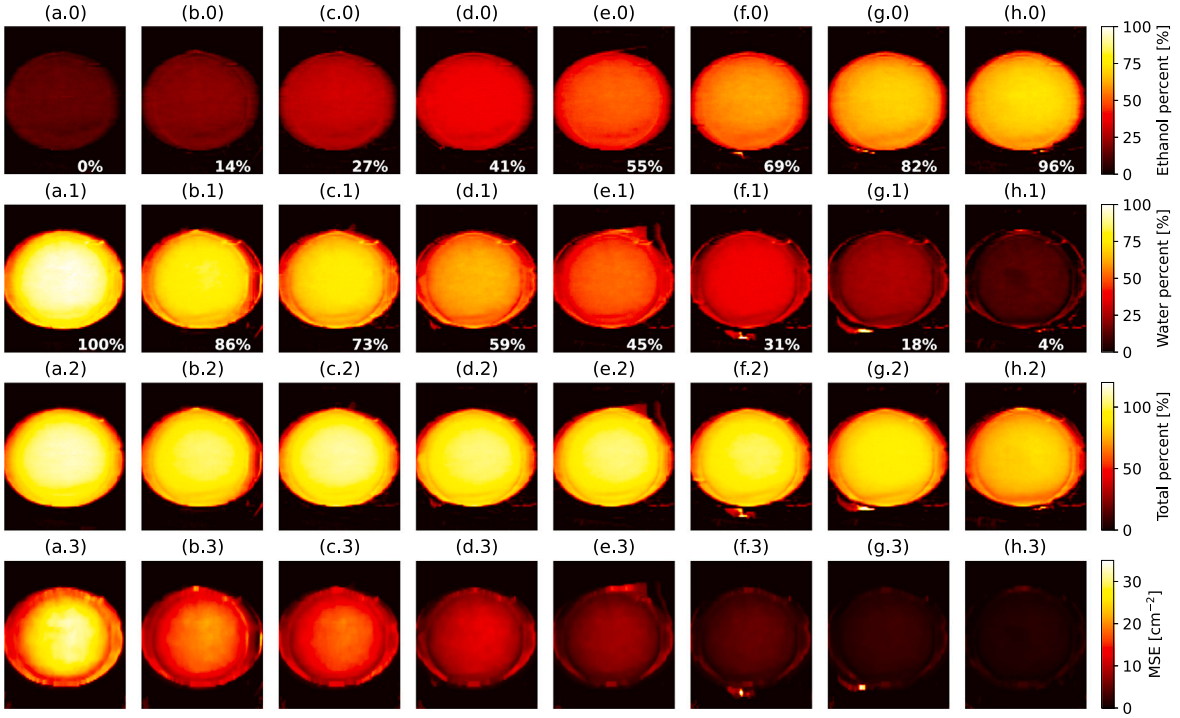

Fig. 11. Results of concentration measurements using average coefficients. The images have been labeled following Fig. 4: (a.0-h.0) ethanol concentrations; (a.1-h.1) water concentrations; (a.2-h.2) concentrations of the ethanol and water mixture; (a.3-h.3) MSE (Mean Squared Error) of the absorption coefficient fit to Eq. (20). Each row has its own colorbar, which is shared across all images within that row.

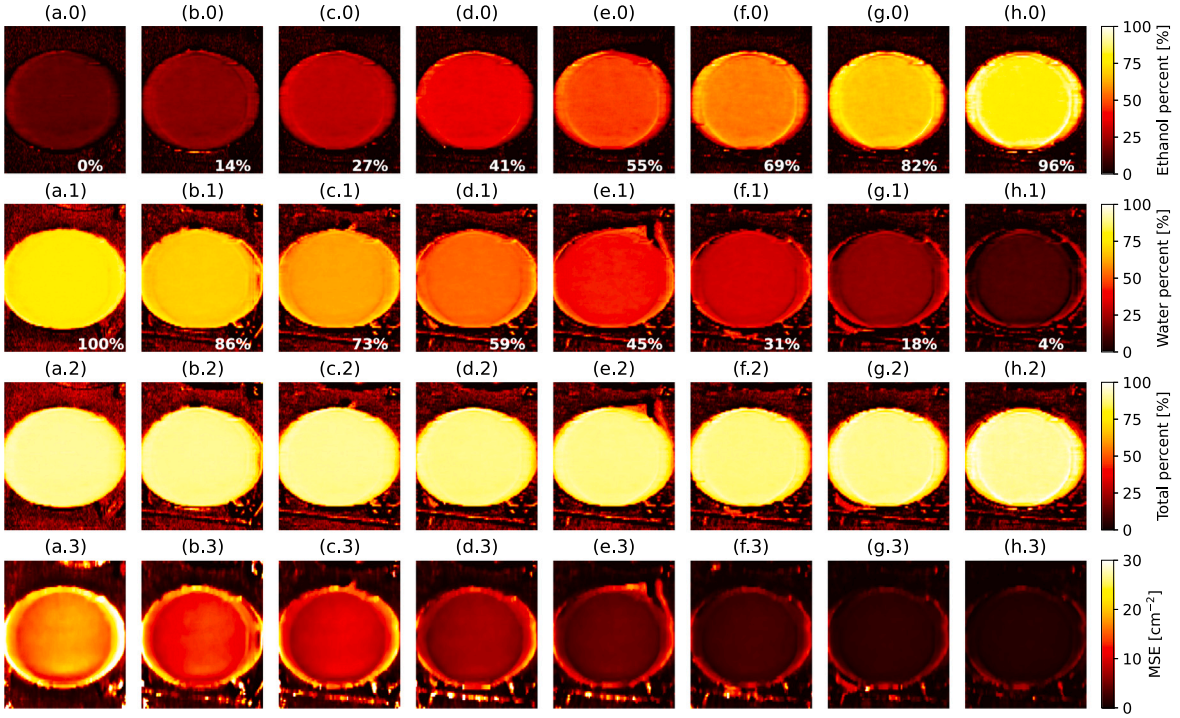

Fig. 12. Results of concentration measurements using pixel-wise coefficients. The images have been labeled following Fig. 4: (a.0-h.0) ethanol concentrations; (a.1-h.1) water concentrations; (a.2-h.2) concentrations of the ethanol and water mixture; (a.3-h.3) MSE (Mean Squared Error) of the absorption coefficient fit to Eq. (20). Each row has its own colorbar, which is shared across all images within that row.

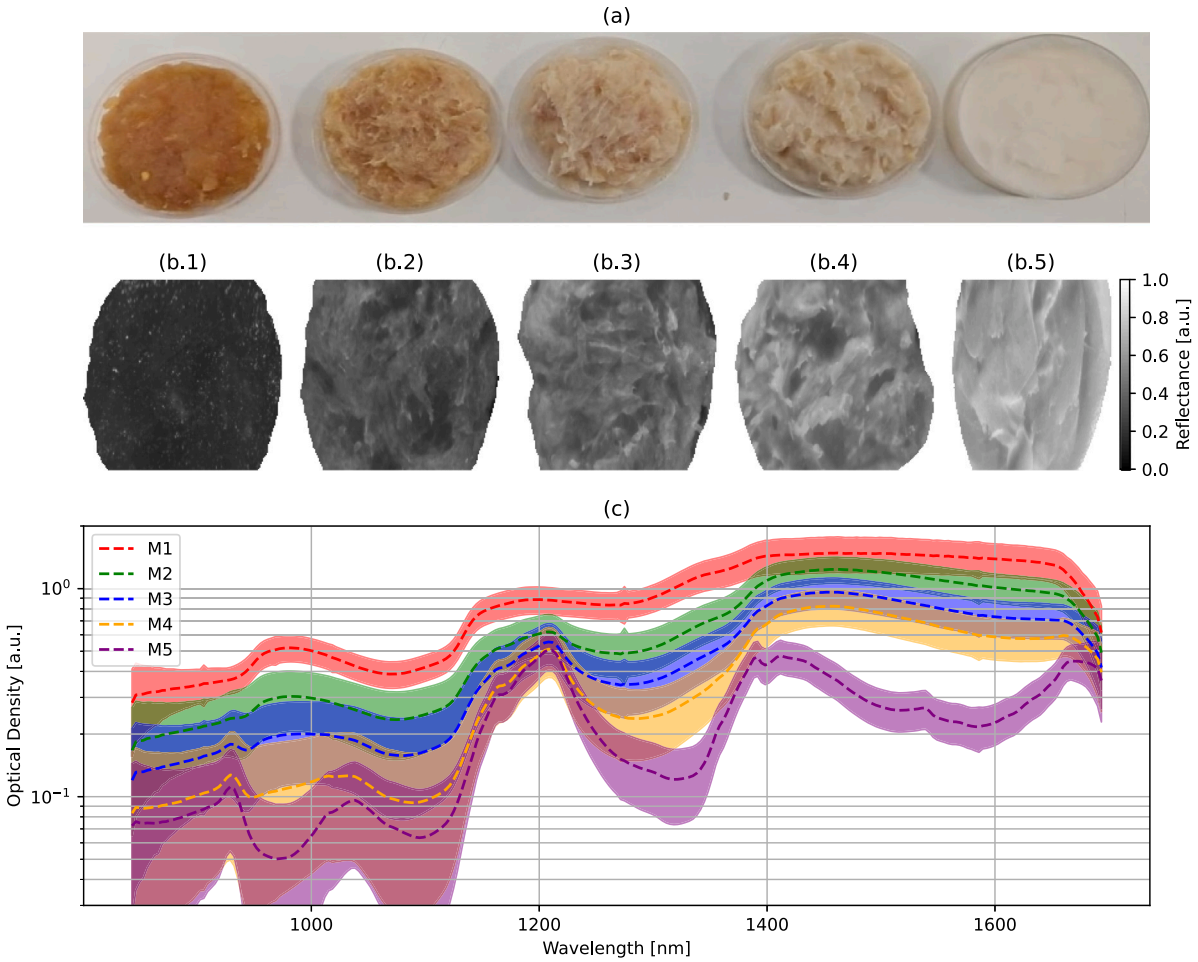

Fig. 13. Results of the chicken meat and pork lard mixtures. (a) RGB photograph of the mixtures, arranged from left to right with increasing fat content; (b) average reflectance map of the mixtures; (c) average spectra and their standard deviation for each mixture (around 195,000 samples per mixture).

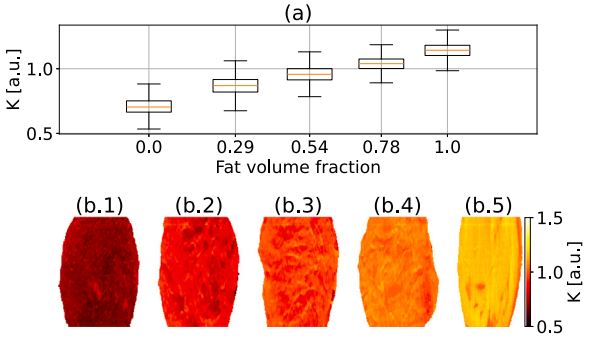

Fig. 14. Results of diffuse reflectance ratios (K) at 970 and 927 nm as a function of fat volume; (a) representation using boxplots; (b) representation in 2D maps.

Furthermore, the proportionality observed suggests that K is sensitive to variations in fat content, making it an indicator for quantifying fat volume in heterogeneous samples. It is observed that, while the pure fat sample appears homogeneous in the RGB image, it exhibits a heterogeneity in the SWIR range similar to the other samples. This occurs because scattering is much higher in the VisNIR range compared to the SWIR range, making fat more easily distinguishable in SWIR.

3.5. Biological tissue

An interesting use case of the HSI-SWIR system involves the measurement of biological samples. In this case, a pork fillet was imaged and two regions were localized within the fillet, one with muscle and another with high fat content.

Fig. 15 contains the results of the pork sample: Fig. 15(a) displays a RGB photograph of the sample taken with a standard camera; Fig. 15(b) shows the average diffuse reflectance with the labeled region of muscle depicted in green and the labeled region of fat depicted in blue; in Fig. 15(c) displays the spectra from the marked areas (green for fat and blue for muscle) and their standard deviations are shown. Vertical lines indicate the wavelengths of 927 and 970 nm. Finally, Fig. 15(d) presents a 2D map of the reflectance ratio between 970 and 927 nm.

When comparing the RGB image with the ratio map, it is observed that the muscle area on the left shows a low ratio, while the upper central region with fat exhibits a high ratio. Additionally, in the central-right area, where fat is visible in the RGB image, the ratio is also high. However, there are areas where fat is not apparent in the RGB image but is detected in the ratio map. This is because the system can detect subcutaneous fat, which a standard imaging system would not be able to identify.

These results demonstrate the potential of the HSI-SWIR system for distinguishing between muscle and fat in biological tissues with high precision by inherently considering sub-surface tissue structures. The ability to penetrate deeper layers of tissue in the SWIR range provides valuable insights that are not apparent in standard RGB imaging. This capability has significant implications for various applications, such as food quality assessment, medical imaging, and the characterization of biological tissues, where accurate differentiation between fat and muscle is critical.

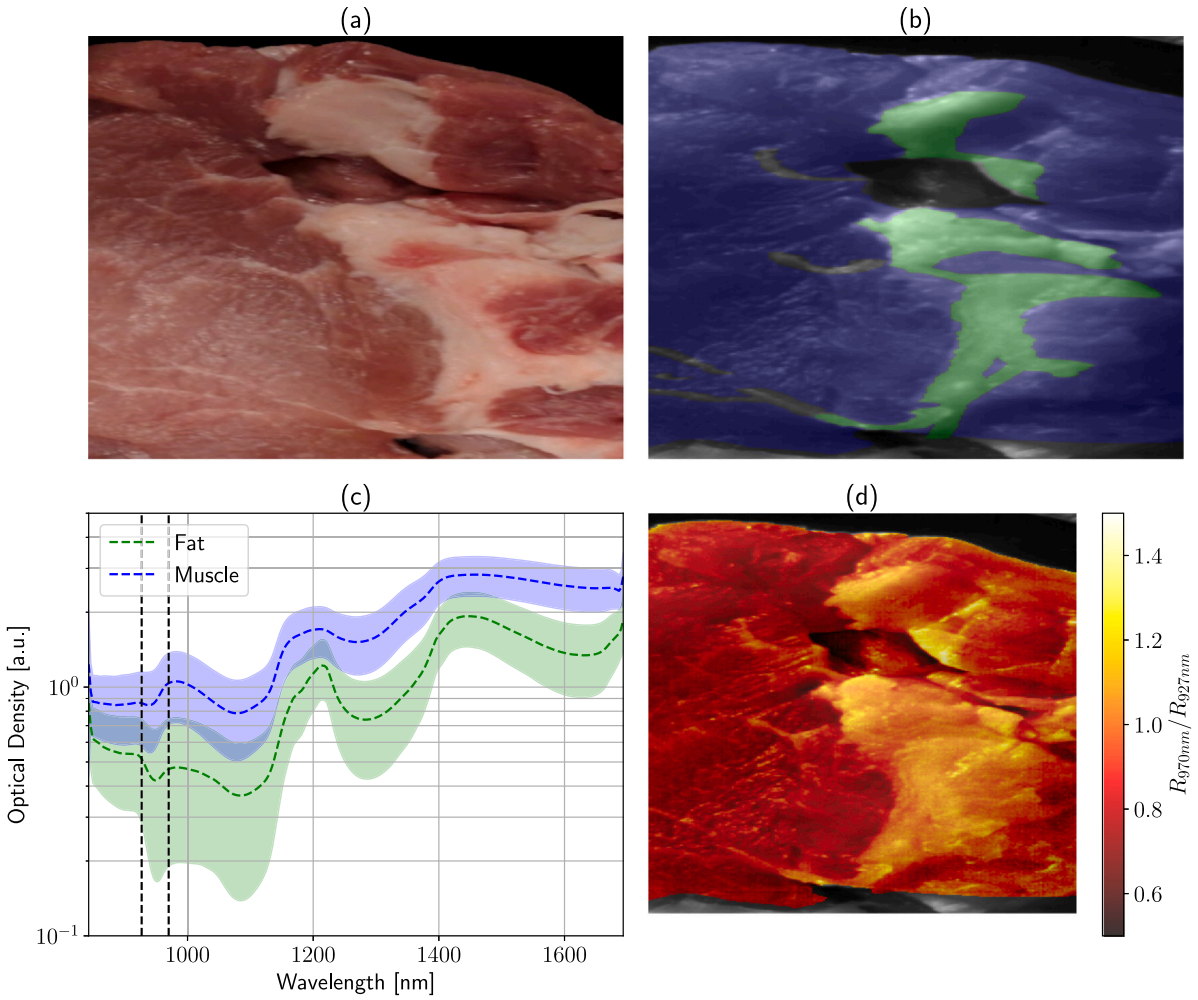

Fig. 15. HSI-SWIR imaging of a pork fillet: (a) RGB image obtained by a photographic camera; (b) average spectral reflectance with two marked regions, muscle (blue) and fat (green); (c) average spectra in the marked regions with their standard deviation (35,967 samples (pixels) of fat, 190,901 samples of muscle); (d) ratio map at 970 and 927 nm.

3.6. Identification of fat content in milk composition

There are scenarios where colorimetric distinction based on RGB or VisNIR device is not enough. An example is determining the fat content in commercial milk to distinguish whether it is whole, semi-skimmed, or skimmed. Milk fat causes significant scattering, giving milk its white and translucent appearance in the VisNIR range. This scattering becomes less noticeable as the wavelength increases, enabling better chemical identification in the SWIR range.

For this experiment, containers, 13.7 mm-height and 28.18 mm-diameter, were filled with whole milk (3.6 g of fat per 100 mL), semi-skimmed milk (1.8 g of fat per 100 mL), and skimmed milk (0.3 g of fat per 100 mL). The containers were measured using both the VisNIR and SWIR systems. Fig. 16(a) shows the nearly flat and overlapping spectra of milk in the VisNIR range. In contrast, Fig. 16(b) shows more pronounced peaks and valleys in the SWIR range with clearly separated spectra between milk categories. While milk fat quantification is possible in the VisNIR range through the characterization of its unique spectral features, the SWIR range simplifies this task considerably by directly providing clear spectral variations associated with the fat concentration.

The results of applying the peak ratio proposed in Eq. (22) are shown in Fig. 17, demonstrating a correlation between the peak ratio and the milk fat content. Additionally, it is important to emphasize that milk and meat differ greatly in both composition and structure, preventing the application of a direct quantitative relationship between the two models.

The use of the SWIR range addresses the limitations of VisNIR systems, particularly in cases where subtle differences in scattering or absorption are not enough to account for fat content levels. Consequently, this spectral range and system are well-suited for applications requiring precise fat quantification, like food quality control or biomedical analysis, where VisNIR range measurements may struggle to provide accurate or reliable results.

4. Conclusion

This work proposes a rotating mirror hyperspectral system operating in the SWIR range. The system provides a high spatial resolution of 176.8×111.36 μm^2, when working with a FoV of 2×10 cm^2 (or 22°), and a spectral resolution of 5 nm, making it able to capture nearly 230 wavelengths in the spectral range of 900 to 1700 nm.

This system performs high-resolution hyperspectral measurements in approximately 30 s to 5 minutes, depending on the chosen scanning resolution and exposure time.

By conducting a preliminary geometrical analysis, it is possible to estimate the concentrations of the various compounds that compose a liquid mixture, provided that their spectra are known. Conversely, the spectra of the samples are estimated if their concentrations are known.

The proposed system also demonstrates its applications in industrial, agri-food, and biomedical fields, as it can identify peaks associated with the presence of its chromophores. Unlike the VisNIR range, where scattering is more pronounced, the SWIR range is less affected scattering,

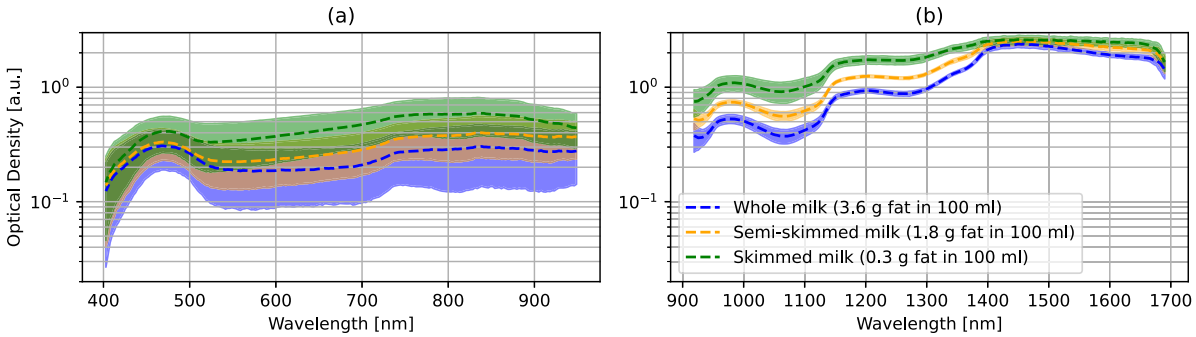

Fig. 16. Spectrum of whole milk, semi-skimmed milk, and skimmed milk: (a) spectra in VisNIR range; (b) spectra in SWIR range. The shaded area indicates the standard deviation (around 35,000 samples per milk type).

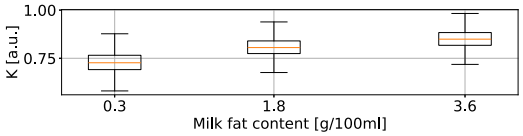

Fig. 17. Results of reflectance ratios at two different wavelengths as a function of fat content in milk at 970 and 927 nm.

enabling deeper penetration into the samples. This greater penetration highlights properties that remain hidden in the VisNIR range.

Furthermore, the SWIR system has proven capable of detecting small variations in concentrations, particularly distinguishing the amount of fat content present in milk.

All these features, combined with its imaging capability, enable numerous applications that are beyond the reach of the VisNIR range. Additionally, the proposed system's semi-portable design allows it to be transported to various locations for in-situ measurements.

CRediT authorship contribution statement

José A. Gutiérrez-Gutiérrez: Writing – original draft, Visualization, Validation, Software, Methodology, Investigation, Formal analysis, Data curation, Conceptualization. **Verónica Mieites:** Writing – review & editing, Visualization, Validation, Methodology, Investigation, Formal analysis, Data curation, Conceptualization. **José M. López-Higuera:** Resources, Project administration, Funding acquisition. **Olga M. Conde:** Writing – review & editing, Supervision, Resources, Project administration, Methodology, Funding acquisition, Formal analysis, Conceptualization.

Funding

Support for this work was provided by the projects PREVAL 21/07 (FUSIOMUSCLE), SUBVTC-2021-0038 (HYPERfusionTRANS), DTS22/ 00127 (hyPERfusioCAM), PERFORMANCE (PID2022-137269OB-C22 financiado por MCIN/ AEI/10.13039/501100011033/ *y* por FEDER Una manera de hacer Europa), DTS17-00055 (INTRACARDIO) and DISFOS (PID2019-107270RB-C21 /AEI/ 10.13039/501100011033), financed by the ISCIII, the Fundación Instituto de Investigación Valdecilla (IDIVAL), Spain and the Spanish Ministry of Science, Innovation and Universities, co-financed with FEDER funds.

Declaration of competing interest

The authors declare that they have no known competing financial interests or personal relationships that could have appeared to influence the work reported in this paper.

Acknowledgments

The authors would like to thank Dr. Arturo Pardo for his contributions to the design and development of the hyperspectral system throughout the duration of his Ph.D. program at Universidad de Cantabria.

Data availability

Data will be made available on request.

References

[1] R. Pu, Hyperspectral Remote Sensing: Fundamentals and Practices, first ed., Boca Raton, FL, USA, CRC Press, 2017.

[2] R.H. Wilson, K.P. Nadeau, F.B. Jaworski, B.J. Tromberg, A.J. Durkin, Review of short-wave infrared spectroscopy and imaging methods for biological tissue characterization, J. Biomed. Opt. 20 (3) (2015) 030901, http://dx.doi.org/10.1117/1.jbo.20.3.030901.

[3] P. Barnabé, G. Dislaire, S. Leroy, E. Pirard, Design and calibration of a two-camera (visible to near-infrared and short-wave infrared) hyperspectral acquisition system for the characterization of metallic alloys from the recycling industry, J. Electron. Imaging 24 (6) (2015) 061115, http://dx.doi.org/10.1117/1.jei.24.6.061115.

[4] M. Oh, H. Lee, I. Torres, A. Garrido Varo, D. Pérez Marín, M.S. Kim, Analysis of pork and poultry meat and bone meal mixture using hyperspectral imaging, in: Sensing for Agriculture and Food Quality and Safety IX, vol. 10217, SPIE, 2017-05-01, p. 102170K, http://dx.doi.org/10.1117/12.2263674.

[5] N. Wu, H. Jiang, Y. Bao, C. Zhang, J. Zhang, W. Song, Y. Zhao, C. Mi, Y. He, F. Liu, Practicability investigation of using near-infrared hyperspectral imaging to detect rice kernels infected with rice false smut in different conditions, Sens. Actuators B: Chem. 308 (2020) 127696, http://dx.doi.org/10.1016/j.snb.2020.127696.

[6] C. Wakholi, L.M. Kandpal, H. Lee, H. Bae, E. Park, M.S. Kim, C. Mo, W.-H. Lee, B.-K. Cho, Rapid assessment of corn seed viability using short wave infrared line-scan hyperspectral imaging and chemometrics, Sens. Actuators B: Chem. 255 (2018) 498–507, http://dx.doi.org/10.1016/j.snb.2017.08.036.

[7] S. Shrestha, M. Knapič, U. Žibrat, L.C. Deleuran, R. Gislum, Single seed near-infrared hyperspectral imaging in determining tomato (Solanum Lycopersicum L.) seed quality in association with multivariate data analysis, Sens. Actuators B: Chem. 237 (2016-12) 1027–1034, http://dx.doi.org/10.1016/j.snb.2016.08.170.

[8] L.M. Kandpal, S. Lohumi, M.S. Kim, J.-S. Kang, B.-K. Cho, Near-infrared hyperspectral imaging system coupled with multivariate methods to predict viability and vigor in muskmelon seeds, Sens. Actuators B: Chem. 229 (2016-06) 534–544, http://dx.doi.org/10.1016/j.snb.2016.02.015.

[9] N. Susič, U. Žibrat, S. Širca, P. Strajnar, J. Razinger, M. Knapič, A. Vončina, G. Urek, B. Gerič Stare, Discrimination between abiotic and Biotic drought stress in tomatoes using hyperspectral imaging, Sens. Actuators B: Chem. 273 (2018-11) 842–852, http://dx.doi.org/10.1016/j.snb.2018.06.121.

[10] E. Park, S. Lohumi, B.-K. Cho, Line-scan imaging analysis for rapid viability evaluation of white-fertilized-egg embryos, Sens. Actuators B: Chem. 281 (2019-02) 204–211, http://dx.doi.org/10.1016/j.snb.2018.10.109.

[11] H. Lee, M.S. Kim, S. Lohumi, B.-K. Cho, Detection of melamine in milk powder using MCT-based short-wave infrared hyperspectral imaging system, Food Addit. Contam.: Part A 35 (6) (2018) 1027–1037, http://dx.doi.org/10.1080/19440049.2018.1469050.

[12] C. Cucci, E.K. Webb, A. Casini, M. Ginanni, E. Prandi, L. Stefani, T. Vitorino, M. Picollo, Short-wave infrared reflectance hyperspectral imaging for painting investigations: A methodological study, J. Am. Inst. Conserv. 58 (1–2) (2019) 16–36, http://dx.doi.org/10.1080/01971360.2018.1543102.

[13] J. Tversky, D. MacGlashan, Short-wave infrared camera as a novel solution to allergy skin testing, Allergy 75 (4) (2019) 965–968, http://dx.doi.org/10.1111/all.14089.

[14] T. Du, D.K. Mishra, L. Shmuylovich, A. Yu, H. Hurbon, S.T. Wang, M.Y. Berezin, Hyperspectral imaging and characterization of allergic contact dermatitis in the short-wave infrared, J. Biophotonics 13 (9) (2020) http://dx.doi.org/10.1002/jbio.202000040.

[15] M.R. Kutteruf, M.K. Yetzbacher, M.J. Deprenger, K.M. Novak, C.A. Miller, A. Kanaev, 9-band SWIR multispectral sensor providing full-motion video, in: D.J. Henry, D.A. Lange, D. Linne von Berg, S.D. Rajan, T.J. Walls, D.L. Young (Eds.), Airborne Intelligence, Surveillance, Reconnaissance (ISR) Systems and Applications XI, SPIE, 2014, http://dx.doi.org/10.1117/12.2049975.

[16] H. Steiner, S. Sporrer, A. Kolb, N. Jung, Design of an active multispectral SWIR camera system for skin detection and face verification, J. Sensors 2016 (2016) 1–16, http://dx.doi.org/10.1155/2016/9682453.

[17] B.J. Orr, Y. He, Tunable nonlinear-optical devices for laser-spectroscopic sensing, in: P.E. Powers (Ed.), in: Nonlinear Frequency Generation and Conversion: Materials, Devices, and Applications IX, vol. 7582, SPIE, International Society for Optics and Photonics, 2010, p. 75820J, http://dx.doi.org/10.1117/12.840867.

[18] W. Wang, C. Li, E.W. Tollner, G.C. Rains, R.D. Gitaitis, A liquid crystal tunable filter based shortwave infrared spectral imaging system: Calibration and characterization, Comput. Electron. Agric. 80 (2012) 135–144, http://dx.doi.org/10.1016/j.compag.2011.09.003.

[19] H. Fabelo, S. Ortega, R. Lazcano, D. Madroñal, G. M. Callicó, E. Juárez, R. Salvador, D. Bulters, H. Bulstrode, A. Szolna, J. Piñeiro, C. Sosa, A. J. O'Shanahan, S. Bisshopp, M. Hernández, J. Morera, D. Ravi, B. Kiran, A. Vega, A. Báez-Quevedo, G.-Z. Yang, B. Stanciulescu, R. Sarmiento, An intraoperative visualization system using hyperspectral imaging to aid in brain tumor delineation, Sensors 18 (2) (2018) 430, http://dx.doi.org/10.3390/s18020430.

[20] N. Hagen, M.W. Kudenov, Review of snapshot spectral imaging technologies, Opt. Eng. 52 (9) (2013) 090901, http://dx.doi.org/10.1117/1.oe.52.9.090901.

[21] M.H. Tran, B. Fei, Compact and ultracompact spectral imagers: technology and applications in biomedical imaging, J. Biomed. Opt. 28 (04) (2023) http://dx.doi.org/10.1117/1.jbo.28.4.040901.

[22] J. Gutiérrez-Gutiérrez, A. Pardo, E. Real, J. López-Higuera, O.M. Conde, Custom scanning hyperspectral imaging system for biomedical applications: Modeling, benchmarking, and specifications, Sensors 19 (2019) 1692, http://dx.doi.org/10.3390/s19071692.

[23] K. Cluff, G. Naganathan, J. Subbiah, R. Lu, C. Calkins, A. Samal, Optical scattering in beef steak to predict tenderness using hyperspectral imaging in the VIS-NIR region, Sens. Instrumen. Food Qual. 2 (2008) 189–196, http://dx.doi.org/10.1007/s11694-008-9052-2.

[24] J. Mirapeix, A. Cobo, A.M. Cubillas, O.M. Conde, J.M. Lopez-Higuera, In-process automatic wavelength calibration for CCD-spectrometers, in: F. Berghmans, A.G. Mignani, A. Cutolo, P.P. Meyrueis, T.P. Pearsall (Eds.), in: Optical Sensors 2008, vol. 7003, SPIE, International Society for Optics and Photonics, 2008, p. 70031T, http://dx.doi.org/10.1117/12.781040.

[25] J. Popp, V.V. Tuchin, A. Chiou, Handbook of Biophotonics, Wiley-VCH, 2012.

[26] S.K.V. Sekar, I. Bargigia, A.D. Mora, P. Taroni, A. Ruggeri, A. Tosi, A. Pifferi, A. Farina, Diffuse optical characterization of collagen absorption from 500 to 1700 nm, J. Biomed. Opt. 22 (1) (2017) 015006, http://dx.doi.org/10.1117/1.jbo.22.1.015006.

[27] M. Marois, S.L. Jacques, K.D. Paulsen, Optimal wavelength selection for optical spectroscopy of hemoglobin and water within a simulated light-scattering tissue, J. Biomed. Opt. 23 (7) (2018) 1–5, http://dx.doi.org/10.1117/1.JBO.23.7.071202.

[28] E. Sani, A. Dell'Oro, Spectral optical constants of ethanol and isopropanol from ultraviolet to far infrared, Opt. Mater. 60 (2016) 137–141, http://dx.doi.org/10.1016/j.optmat.2016.06.041.

[29] G.M. Hale, M.R. Querry, Optical constants of water in the 200nm to 200 micron wavelength region, Appl. Opt. 12 (1973) 555–563.

[30] G.C. Holst, T.S. Lomheim, CMOS/CCD Sensors and Camera Systems, second ed., SPIE Press, 2011.

[31] S. Kedenburg, M. Vieweg, T. Gissibl, H. Giessen, Linear refractive index and absorption measurements of nonlinear optical liquids in the visible and near-infrared spectral region, Opt. Mater. Express 2 (11) (2012) 1588–1611, http://dx.doi.org/10.1364/OME.2.001588.

[32] S.L. Jacques, Optical properties of biological tissues: a review, Phys. Med. Biol. 58 (11) (2013) R37–R61, http://dx.doi.org/10.1088/0031-9155/58/11/r37.

[33] G.M. Hale, M.R. Querry, Optical constants of water in the 200-Nm to 200-Um Wavelength Region, Appl. Opt. 12 (3) (1973) 555, http://dx.doi.org/10.1364/AO.12.000555.

[34] X. Zhang, J. Qiu, X. Li, J. Zhao, L. Liu, Complex refractive indices measurements of polymers in visible and near-infrared bands, Appl. Opt. 59 (8) (2020) 2337, http://dx.doi.org/10.1364/AO.383831.

[35] S.K.V. Sekar, I. Bargigia, A.D. Mora, P. Taroni, A. Ruggeri, A. Tosi, A. Pifferi, A. Farina, Diffuse optical characterization of collagen absorption from 500 to 1700ñm, J. Biomed. Opt. 22 (1) (2017) 015006, http://dx.doi.org/10.1117/1.jbo.22.1.015006.

[36] E. Sani, A. Dell'Oro, Spectral optical constants of ethanol and isopropanol from ultraviolet to far infrared, Opt. Mater. 60 (2016-10-01) 137–141, http://dx.doi.org/10.1016/j.optmat.2016.06.041.

[37] S.L. Jacques, Optical properties of biological tissues: a review, Phys. Med. Biol. 58 (11) (2013) R37–R61, http://dx.doi.org/10.1088/0031-9155/58/11/r37.

[38] D.J. Birnkrant, K. Bushby, C.M. Bann, S.D. Apkon, A. Blackwell, D. Brumbaugh, L.E. Case, P.R. Clemens, S. Hadjiyannakis, S. Pandya, N. Street, J. Tomezsko, K.R. Wagner, L.M. Ward, D.R. Weber, Diagnosis and management of duchenne muscular dystrophy, part 1: diagnosis, and neuromuscular, rehabilitation, endocrine, and gastrointestinal and nutritional management, Lancet Neurol. 17 (3) (2018) 251–267, http://dx.doi.org/10.1016/s1474-4422(18)30024-3.

[39] E. Bossone, K.A. Eagle, Epidemiology and management of aortic disease: aortic aneurysms and acute aortic syndromes, Nat. Rev. Cardiol. 18 (5) (2020) 331–348, http://dx.doi.org/10.1038/s41569-020-00472-6.

[40] J.A. Gutiérrez Gutiérrez, V. Mieites, A. Pontón, I. García Montesinos, J.M. López Higuera, O.M. Conde, Evaluation of cardiovascular pathologies in human aortas with hyperspectral imaging and optical coherence tomography, in: D.S. Elson, S. Gioux, B.W. Pogue (Eds.), Clinical Biophotonics III, SPIE, 2024, http://dx.doi.org/10.1117/12.3022425.

[41] N. Chalasani, Z. Younossi, J.E. Lavine, M. Charlton, K. Cusi, M. Rinella, S.A. Harrison, E.M. Brunt, A.J. Sanyal, The diagnosis and management of nonalcoholic fatty liver disease: Practice guidance from the American association for the study of liver diseases, Hepatology 67 (1) (2017) 328–357, http://dx.doi.org/10.1002/hep.29367.

[42] R. Nachabé, B.H.W. Hendriks, A.E. Desjardins, M. van der Voort, M.B. van der Mark, H.J.C.M. Sterenborg, Estimation of lipid and water concentrations in scattering media with diffuse optical spectroscopy from 900 to 1600 nm, J. Biomed. Opt. 15 (3) (2010) 037015, http://dx.doi.org/10.1117/1.3454392.

[43] W.C. Etchison, Letter to the editor response, Sport. Heal. 3 (6) (2011) 499, http://dx.doi.org/10.1177/1941738111422691.

[44] M.I. Ochoa, A. Ruiz, E. LaRochelle, M. Reed, E. Berber, G. Poultsides, B.W. Pogue, Assessment of open-field fluorescence guided surgery systems: implementing a standardized method for characterization and comparison, J. Biomed. Opt. 28 (09) (2023) http://dx.doi.org/10.1117/1.jbo.28.9.096007.

[45] M. Born, E. Wolf, Principles of Optics: Electromagnetic Theory of Propagation, Interference and Diffraction of Light, seventh expanded ed., Cambridge University Press, 1999.

[46] S.-C. Yoon, B. Park, K. Lawrence, W. Windham, G. Heitschmidt, Line-scan hyperspectral imaging system for real-time inspection of poultry carcasses with fecal material and ingesta, Comput. Electron. Agric. 79 (2011) 159–168, http://dx.doi.org/10.1016/j.compag.2011.09.008.

José A. Gutiérrez-Gutiérrez: was born in 1990 in Santander. He obtained a Master's degree in Telecommunications Engineering in July 2018 and his Ph.D. in 2024 from the University of Cantabria. His thesis research work is carried out within the Photonic Engineering Group, focused mainly on transferring spectroscopy systems to a real clinical environment, the calibration of these equipments and their fine-tuning.

Verónica Mieites: B.Sc. in Physics (2019) from University of Santiago de Compostela and M.Sc. in Science and Engineering of Light (2020) from University of Cantabria, is currently a Ph.D. candidate at the same university. Her work involves both the measurement of biological tissues by means of optical coherence tomography (OCT), hyperspectral imaging (HSI) systems and polarimetric imaging techniques, and the subsequent analysis and processing of these measurements. The purpose of these measurements is to obtain information for the diagnosis of the analyzed biological tissues, in a fast and non-invasive way.

José M. López-Higuera: He was born in Ramales de la Victoria, Cantabria, Spain, in February 1954. He received the Telecommunication Technical Engineering degree from the Universidad Laboral de Alcala de Henares, Madrid, Spain, and the Telecommunication Engineering and Ph.D. degrees in telecommunication engineering from the Universidad Politecnica de Madrid, Madrid, Spain. He founded and is currently the Head of the Photonics Engineering Group, TEISA Department, University of Cantabria, Santander, Spain. He works in the development of photonics instrumentation, photonic/optical fiber sensor systems for civil engineering, electrical power, environmental and smart structures, and for optical diagnostics for a wide range of applications. He has directed more than 50 research and development projects and has authored or coauthored more than 400 publications in the form of books, chapters of books, papers, and conferences, both national and international, and holds ten patents. He is the Editor and the coauthor of several books, including Optical Sensors, UC, 1998 and Handbook of Optical Fibre Sensing Technology, Wiley, 2002. He is the Co-Editor of the book Engineering a High-Tech Business: Entrepreneurial Experiences and Insights,

SPIE-Press, 2008. He is a Member of the IEE, SPIE, and OSA. He was the recipient of the Extraordinary Ph.D. Award.

Olga M. Conde: Ms. Eng. (1994) and Ph.D. (1999) in Telecommunications Engineering from the University of Cantabria. Associate Professor since 1999 in the Photonics Engineering Group of the University of Cantabria, IDIVAL (Marques de Valdecilla Biomedical Research Institute) and CIBER-BBN (Bioengineering, Biomaterials and Nanomedicine Networking Biomedical Research Centre). Her research interests are focused on medical imaging techniques for tumor delineation (breast, melanoma, pancreas, glioma) and diagnosis of cardiovascular pathologies (aneurysm, hearth valve repair surgery); artificial intelligence (pattern and features recognition techniques, spectral analysis, etc.) applied to artificial vision and imaging spectroscopy for biomedical, agri-food and industrial environments; development of spectroscopic/hyperspectral imaging systems for materials in the visible, NIR and SWIR ranges. Her research is funded by the Institute of Health Carlos III and the Ministry of Economy and Competitiveness publishing over 50 peer-reviewed papers and over 180 conference papers. She is vicepresident of the Imaging Techniques Committee of SEDOPTICA (Spanish Optical Society), member of the TPC (Technical Program Committee) and IAB (International Advisory Board) of different conferences (SPIE, OSA, IEEE, LALS) and reviewer of evaluation agencies ANEP (Spanish National Agency for Evaluation and Forecasting) and FNRS (Belgium Fund for Scientific Research) and different scientific journals.